



Direct observation of nonequivalent Fermi-arc states of opposite surfaces in the noncentrosymmetric Weyl semimetal NbP

S. Souma,¹ Zhiwei Wang,² H. Kotaka,² T. Sato,³ K. Nakayama,³ Y. Tanaka,³ H. Kimizuka,³ T. Takahashi,^{1,3} K. Yamauchi,² T. Oguchi,² Kouji Segawa,⁴ and Yoichi Ando^{2,5}

¹WPI Research Center, Advanced Institute for Materials Research, Tohoku University, Sendai 980-8577, Japan

²Institute of Scientific and Industrial Research, Osaka University, Ibaraki, Osaka 567-0047, Japan

³Department of Physics, Tohoku University, Sendai 980-8578, Japan

⁴Department of Physics, Kyoto Sangyo University, Kyoto 603-8555, Japan

⁵Institute of Physics II, University of Cologne, Köln 50937, Germany

(Received 6 October 2015; revised manuscript received 5 March 2016; published 20 April 2016)

We have performed high-resolution angle-resolved photoemission spectroscopy (ARPES) on noncentrosymmetric Weyl semimetal candidate NbP, and determined the electronic states of both Nb- and P-terminated surfaces. We revealed a drastic difference in the Fermi-surface topology between two types of surfaces, whereas the Fermi arcs on both surfaces are likely terminated at the surface projection of the same bulk Weyl nodes. A comparison of the ARPES data with our first-principles band calculations suggests a notable difference in the electronic structure at the Nb-terminated surface between theory and experiment. The present result opens a platform for realizing exotic quantum phenomena arising from the unusual surface properties of Weyl semimetals.

DOI: [10.1103/PhysRevB.93.161112](https://doi.org/10.1103/PhysRevB.93.161112)

Weyl semimetals (WSMs) manifest a novel quantum state of matter where the bulk conduction and valence bands cross at discrete points with linear dispersion in all the momentum (\mathbf{k}) directions in a three-dimensional (3D) Brillouin zone (BZ), which can be viewed as a 3D analog of graphene breaking time-reversal or space-inversion symmetry [1–9]. The band-crossing point is called the Weyl node that is effectively described by the Weyl equation [1,2,6], and is robust against perturbations expressed in terms of Pauli matrices. The Weyl node always comes in pairs acting as a monopole (source) or antimonopole (sink) of Berry curvature in \mathbf{k} space, associated with positive or negative chirality, respectively [10,11]. The WSMs can host many exotic physical phenomena such as anomalous Hall effects, chiral anomalies [12,13], and magnetoelectric effects [14–17].

The most intriguing prediction for WSMs is the emergence of Fermi arcs on their surfaces. Unlike 2D metals showing *closed* Fermi-surface (FS) pockets, the Fermi arcs in WSMs are disjoint, *open* curves [see Fig. 1(a)]; they must start and end at the projections of a pair of bulk Weyl cones of opposite chiralities onto the surface BZ, independent of surface orientations and terminations. The shape of the Fermi arcs in two opposite surfaces in WSMs is not equivalent with each other due to the breaking of time-reversal or inversion symmetry. Such a surface state is a characteristic of WSMs, leading to the predictions of intriguing phenomena such as quantum interference [18] and quantum oscillations [19], in which the propagation of electrons across the top and bottom surfaces through the bulk plays an essential role. Thus, a simultaneous consideration of both surfaces is necessary to understand the unusual physical properties of WSMs.

Recently, density functional theory predicted that transition-metal monpnictide family TaAs, TaP, NbAs, and NbP are WSMs with 12 pairs of Weyl nodes in bulk BZ [20,21]. These compounds crystallize in a noncentrosymmetric structure [the $I4_1md$ space group; Fig. 1(b)], distinct from the WSM candidates which break time-reversal symmetry [1,4,5]. Angle-resolved photoemission spectroscopy (ARPES) of

monpnictides, in particular, TaAs, confirmed the existence of Fermi arcs on anion-terminated surfaces and bulk Weyl nodes [22–29], consistent with the theoretical prediction. To firmly establish the WSM nature of monpnictides and to build a basis for the proposed exotic phenomena, it is of particular importance to experimentally establish the fermiology of both surfaces.

In this Rapid Communication, we report ARPES results on NbP in which ultrahigh carrier mobility and extremely large magnetoresistance [30,31] were recently reported. We determined the electronic states of both Nb- and P-terminated surfaces. At the P-terminated surface, we observed a tadpole-shaped FS at the BZ corner, whereas such a signature is absent at the Nb-terminated counterpart, demonstrating nonequivalent electronic states between two types of surfaces. We discuss the implications of our findings in terms of the bulk Weyl nodes and physical properties related to the surface Fermi arc of WSMs.

We have carried out first-principles band calculations (see Sec. 3 of the Supplemental Material [32] for details), and confirmed that NbP is a WSM with two kinds of Weyl-node pairs W1 and W2 [20,21,33] [see Fig. 1(c)]. The Weyl-cone-like dispersion is recognized from the bulk bands in Figs. 1(d) and 1(e) calculated along cuts crossing W1 or W2.

At first we explain how to distinguish the Nb- and P-terminated surfaces. NbP crystal has two possible cleaving planes, as indicated by the dashed or solid arrows in Fig. 1(b). Among these, the cleave occurs easier by breaking two Nb-P bonds per unit cell (orange line) [24,25,33], rather than by breaking four bonds (dashed line), which is supported by our atomic-force-microscopy measurements (see Sec. 2 of the Supplemental Material for details). This is also consistent with our calculations in which a slab with a fourfold coordinated surface is 2.5 eV per unit cell more stable than that with twofold coordination. Therefore, when we cleave the surface with the [001] axis directed upward as in Fig. 1(b), the Nb-terminated (001) surface must always appear. This in return indicates that the other side of the crystal, i.e., the (00 $\bar{1}$) surface, is

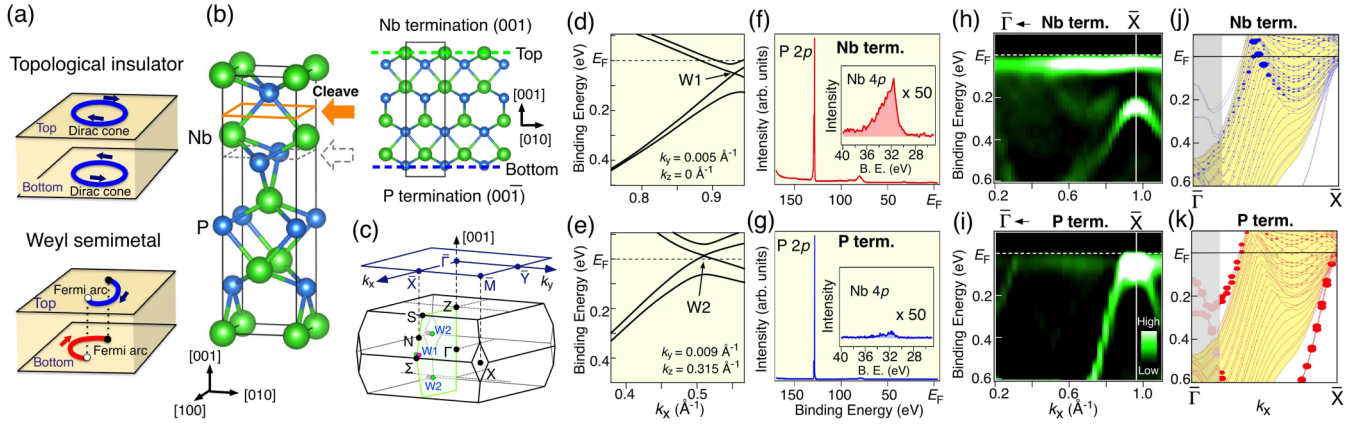


FIG. 1. (a) Schematics of the Dirac-cone and Fermi-arc surface states at opposite surfaces of the topological insulator (top) and WSM (bottom), respectively. (b) Left: Crystal structure of NbP with two possible cleaving planes (arrows). Right: Side view of the crystal structure. (c) Bulk and surface BZs of NbP. The green shaded area is a mirror plane which is projected onto the $\bar{\Gamma}\bar{X}$ line, and red and green dots highlight the Weyl nodes (W1, W2). (d), (e) Calculated bulk-band dispersion along cuts crossing W1 and W2, respectively. (f), (g) ARPES spectrum measured at $h\nu = 200$ eV for the Nb- and P-terminated surfaces, respectively. (h), (i) Second derivative of ARPES intensity along $\bar{\Gamma}\bar{X}$ cut for the Nb- and P-terminated surfaces, respectively. (j), (k) Calculated band structure for a slab of 7-unit-cell NbP, for Nb- and P-terminated surfaces, respectively. The radius of circles represents the surface spectral weight. The projection of bulk bands is shown by the yellow shade. The gray shaded area is outside of the band plots in (h) and (i).

P terminated. In this regard, it can be said that the P- and Nb-terminated surfaces are “opposite” surfaces. Two such terminations do not coexist on a single cleaved surface as long as the crystal is composed of a single domain. We accumulated the ARPES data for many cleaves, and confirmed that the obtained data are always classified into two categories attributed to either the Nb-terminated or the P-terminated surface, suggesting the presence of an easy cleaving plane and the single-domain nature of our crystal.

Figures 1(f) and 1(g) show the energy distribution curve (EDC) of NbP for the Nb- and P-terminated surfaces, respectively, measured with $h\nu = 200$ eV (see Sec. 1 of the Supplemental Material for experimental details). In both surfaces, one can recognize a sharp P $2p$ core-level feature at a binding energy E_B of ~ 130 eV. At $E_B = 32$ eV, we observe another peak originating from the Nb $4p$ core levels (inset) which is apparently weaker for the P-terminated surface [note that the reason why the intensity of Nb $4p$ is much lower than that of P $2p$ in Figs. 1(f) and 1(g) is due to an approximately ten times weaker photoionization cross section of the Nb $4p$ orbital]. Figures 1(h) and 1(i) display a comparison of the ARPES intensity between two terminations along the $\bar{\Gamma}\bar{X}$ cut. At the Nb-terminated surface, there exists a holelike band at \bar{X} which has a top of dispersion at $E_B \sim 0.25$ eV, together with a V-shaped band within 0.3 eV of E_F , whereas at the P-terminated surface, the V-shaped band is absent and a holelike band touches E_F around \bar{X} . As shown by a comparison of experimental and calculated band dispersions in Figs. 1(i) and 1(k), the calculated surface bands reproduce the overall experimental band dispersions for the P-terminated surface, whereas the experimental holelike band away from E_F is hardly reproduced for the Nb-terminated surface [Figs. 1(h) and 1(j)].

We begin with the electronic states of the P-terminated surface. Figure 2(a) displays a schematic summary of the experimentally observed FS of NbP around \bar{X} . The energy

bands labeled here, S_1 – S_4 , all of which are surface states [23], obey different selection rules of photoelectron intensity. For example, band S_1 , which is likely connected to the projection of Weyl pairs W1 and W2 [Fig. 2(a); we will come back to this point later], is dominantly seen at $h\nu = 21$ eV with vertical polarization [Fig. 2(b)]. On the other hand, the intensity of outer band S_2 is greatly enhanced with circularly polarized 50-eV photons [Fig. 2(c)]. The intensity difference is also recognized from a comparison of the band dispersion along cut A in Fig. 2(d) where the distance between the two k_F points (arrows) is wider at $h\nu = 50$ eV than that at 21 eV. Such band behavior also leads to the difference in the FS topology; i.e., S_1 forms a closed pocket away from \bar{X} , as seen from the absence of E_F crossing in cut B, whereas S_2 forms a tadpole FS, as suggested by its E_F crossing in cut B [Fig. 2(d)]. There exist other dog-bone-shaped FSs, S_3 and S_4 , elongated along $\bar{X}\bar{M}$ [Fig. 2(a)], which are better resolved with horizontally polarized 21-eV photons [Fig. 2(e)]. We found that overall the cross-shaped FS in the experiment is reasonably reproduced by our calculation [Fig. 2(f)]. In particular, the \mathbf{k} location of the “head” of the tadpole FS and its narrow “tail” show good correspondence with each other (some differences such as the absence/appearance of S_1 and S_3 pockets can be also recognized).

Now we turn our attention to the electronic structure of the Nb-terminated surface, which has been hardly studied in monpnictides [27]. Figures 3(a) and 3(b) display ARPES-intensity mapping at E_F and the corresponding second-derivative intensity of the EDCs, respectively. At first glance, FS looks very different from that of the P-terminated surface. The cross-shaped FS is absent, and the finite spectral weight is observed around $\bar{\Gamma}$. These differences are not attributable to the simple energy shift between opposite surfaces as visible from several energy slices in Figs. 2(b) and 3(d).

The electron versus holelike nature of the FSs in Fig. 3(c) can be signified by tracing the experimental band dispersion

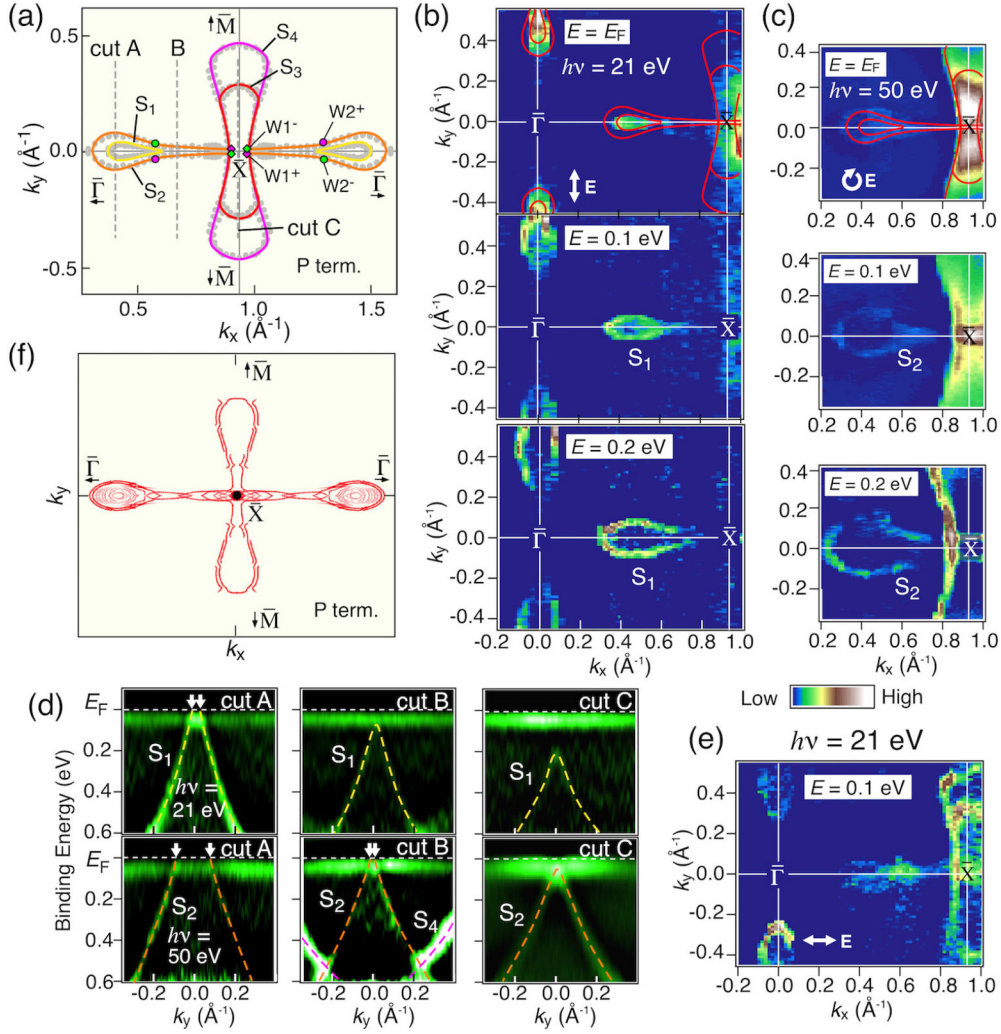


FIG. 2. (a) Experimental FS around \bar{X} for the P-terminated surface. Fermi wave vectors (k_F 's) are plotted with gray dots. The projection of Weyl nodes estimated from the present experiment is also indicated by circles and diamonds. (b) Second-derivative intensity of the EDCs at $E_B = E_F, 0.1$ and 0.2 eV, measured with vertically polarized 21-eV photons. The polarization vector of lights is indicated by the arrow. Experimental FSs are overlaid for $E_B = E_F$. (c) Same as (b) but measured with circularly polarized 50-eV photons. (d) Second-derivative intensity in cuts A–C, measured with $h\nu = 21$ eV (top) and 50 eV (bottom). The dashed curves are a guide to the eyes to trace the band dispersions. (e) Second-derivative intensity at $E_B = 0.1$ eV measured with horizontally polarized lights of $h\nu = 21$ eV. (f) Calculated FS around \bar{X} . The surface weight is reflected by the gradual color scale. The \mathbf{k} window is the same as (a).

at various \mathbf{k} cuts shown in Fig. 3(e). Around $\bar{\Gamma}$, we identify two kinds of FSs arising from bands S_5 and S_6 : Band S_5 forms a circular hole pocket, while band S_6 has an electronlike dispersion centered at $\bar{\Gamma}$, as seen from cuts A, C, and D in Fig. 3(e). Around \bar{X} , we identify a large hole pocket (S_8) with a holelike character (cuts E–G). This large pocket is connected to a small hole pocket S_7 (cut H). We also find a faint signature of anisotropic FS (S_9) elongated along $\bar{\Gamma}\bar{X}$ (the band dispersion can be traced by analyzing the momentum distribution curves, as detailed in Sec. 6 of the Supplemental Material). It is noted that S_8 and S_9 are likely connected to the Weyl pairs, as discussed later (for \mathbf{k} cuts crossing the projection of Weyl nodes, see Sec. 7 of the Supplemental Material).

The FS topology for the Nb-terminated surface is markedly different between experiment and calculation, as visible from Figs. 3(c) and 3(f). In particular, the FS at $\bar{\Gamma}$ is absent in the calculation. Also, the shapes and numbers of FSs around

\bar{X} are different. This is not ascribable to a difference in the doping level between experiment and calculation; possible surface relaxations, reconstructions, and/or enhanced interactions among the surface Nb $4d$ orbitals may need to be considered to explain such differences, as discussed in Secs. 4 and 5 of the Supplemental Material. To further clarify the origin of the differences between experiment and calculation, it would be necessary to determine the surface structural parameters using, e.g., I - V low-energy electron diffraction and surface x-ray diffraction, and carry out the band calculations with an input of these parameters. It would also be useful to perform the ARPES measurements on the transition-metal-terminated surface of other monpnictides and compare the results with the corresponding band calculations to clarify whether or not the discrepancy is a unique feature of NbP.

Now we discuss the characteristics of observed surface states in relation to the location of bulk Weyl nodes. Figure 4(a)

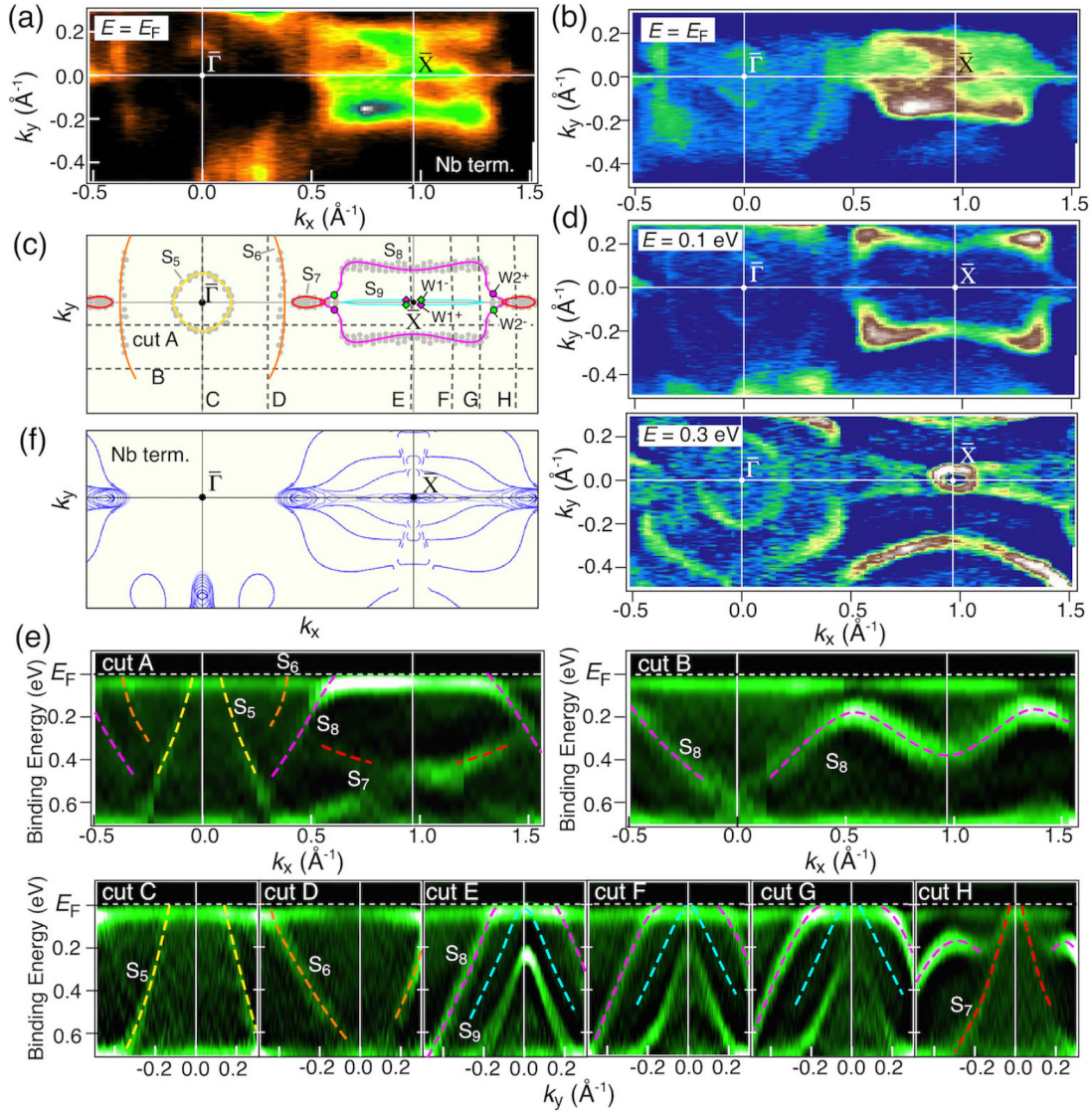


FIG. 3. (a), (b) ARPES-intensity mapping at E_F and second-derivative intensity of the EDCs for the Nb-terminated surface, respectively, plotted as a function of k_x and k_y measured with $h\nu = 50$ eV. (c) Experimental FS for the Nb-terminated surface. k_F points extracted by tracing the band dispersion are plotted with gray dots. The projection of Weyl nodes estimated from the present experiment is also indicated by circles and diamonds. (d) Second-derivative intensity plots of the EDCs at $E_B = 0.1$ and 0.3 eV. (e) Second-derivative intensity along cuts A–H in (c). (f) Calculated FS for the Nb-terminated surface.

summarizes the present ARPES result of NbP, highlighting the significant differences between opposite surfaces. As mentioned above, there exist two kinds of bulk Weyl pairs $W1^\pm$ and $W2^\pm$ (\pm represents the positive/negative chirality) in NbP [20,21,33]. It is expected that Weyl nodes projected onto the (001) or (00 $\bar{1}$) surface terminate two Fermi arcs for $W2$ due to the projection from two pairs, whereas those for $W1$ terminate a single Fermi arc, *independent of surface terminations*. This consideration led us to experimentally pin down the location of Weyl nodes, since the projection of Weyl nodes must appear at (or very close to) the intersection of FSs for opposite surfaces (note that it is essential to determine the electronic structure for both terminations to apply this method, while such a study has not been performed so far in transition-metal monpnictides). While there exist three types of such intersections as indicated by the solid and open

circles in Fig. 4(b), the solid circles are most likely due to the projection of Weyl pair $W2^\pm$, since (i) the calculated distance between adjacent Weyl nodes is wider for $W2$ than that for $W1$ [20,21,33], and (ii) the outer tadpole FS commonly forms a Fermi arc in monpnictides [22–26,28,33] [note that the distance between adjacent Weyl nodes for $W2$ (0.06 \AA^{-1}) is much smaller than that of TaAs ($\sim 0.15 \text{ \AA}^{-1}$) [24], suggesting the essentially weak spin-orbit coupling in NbP]. It turned out to be rather difficult to determine the exact location of the $W1$ pair since the FS for opposite surfaces overlaps with each other around \bar{X} , as visible in Fig. 4(b). Nevertheless, one can conclude that $W1^-$ and $W1^+$ are very close to each other since the FS is nearly on the $\Gamma\bar{X}$ line. In addition, the $W1$ pairs on both sides of \bar{X} are not likely traversed by the FS, since band S_2 appears to sink below E_F along the $\bar{X}\bar{M}$ cut, as shown in cut C of Fig. 2(d). From these arguments, we propose in

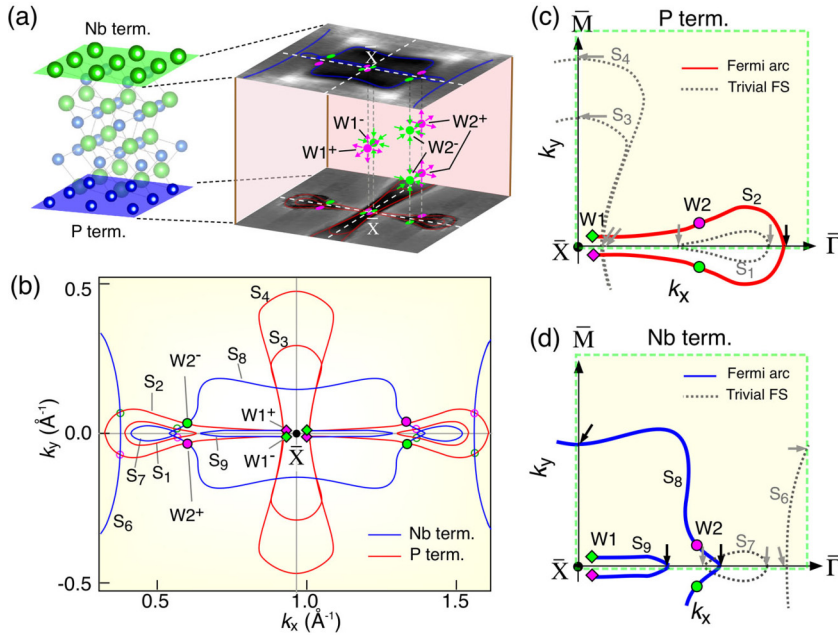


FIG. 4. (a) (Left) crystal structure of NbP and (right) schematics of experimental FS around \bar{X} for the opposite surfaces. Bulk Weyl nodes are illustrated by circles. The arrows indicate the Berry curvature. (b) Direct comparison of experimental FS between Nb-terminated (blue) and P-terminated (red) surfaces. The projection of Weyl nodes W2 at the intersection of FSs for opposite surfaces is overlaid by solid circles, whereas other intersections are shown by open circles. Possible Weyl pairs W1 are also indicated with diamonds. (c), (d) Schematics of Fermi arcs (solid curves) and trivial FSs (gray dashed curves) for the P- and Nb-terminated surfaces, respectively. The closed loop enclosing three Weyl nodes is indicated by a green dashed rectangle. The arrows indicate the crossing points of Fermi arcs and trivial FSs.

Fig. 4(c) the schematic FS for the P-terminated surface which explains most consistently the present ARPES result. The FS (S_2) which connects $W2^\pm$ can be viewed as a combination of two Fermi arcs. Namely, one arc starts and ends at $W2$, and the other is connected to $W1$. It is thus likely that only S_2 forms a Fermi arc and all the others (S_1, S_3, S_4) form a trivial FS. At the Nb-terminated surface [Fig. 4(d)], one Fermi arc (S_8) starts and ends at $W2$, and the other is connected to another $W2$ pair in the opposite k_x region. The Weyl nodes for $W1$ are connected to each other via a single arc S_9 , as inferred from the absence of its FS crossing along $\bar{X}\bar{M}$ [cut E of Fig. 3(e)]. Thus, S_6 and S_7 are likely the trivial FSs. We emphasize, however, that the Fermi-arc connectivity is not unique and depends on the details of the surface [20]; hence, at this stage, the above interpretation is just a likely possibility and its verification requires higher-resolution data.

To examine the WSM nature of NbP, we choose a closed k -loop surrounding the odd number of (three) Weyl nodes and count the total number of FS crossings. Since only an open Fermi arc can cross this loop an odd number of times, the total odd number of FS crossings would be a hallmark of the existence of Fermi arcs in WSM [23,24,28,33]. For the P-terminated surface [Fig. 4(c)], the Fermi arc (S_2) crosses this loop only once, and the trivial FSs (S_1, S_3, S_4) cross six times. For the Nb-terminated surface [Fig. 4(d)], the Fermi arcs (S_8 and S_9) cross this loop three times, and the trivial FSs (S_6 and S_7) cross four times. In either case, the FSs cross the k loop seven times in total, supporting the WSM nature of NbP.

The observed nonequivalent nature of the Fermi arcs between Nb- and P-terminated surfaces suggests a possibility to control the shape of the Fermi arcs by tuning the surface conditions, laying the foundation for the Fermi-arc engineering of WSMs. It is also remarked that the nonequivalence of the surface states should be seriously taken into account in mononictides, as long as the surface transport and spectroscopic properties, such as quantum oscillations in magnetotransport, quasiparticle interference in tunneling spectroscopy, and possible gating devices utilizing ultrathin films, are concerned.

In conclusion, we have reported ARPES results on NbP and elucidated the electronic states of the Nb- and P-terminated surfaces. We revealed that the FS topology is considerably different between these two terminations. We also found that the first-principles calculations hardly reproduce the experimental electronic structure for the Nb-terminated surface, unlike the P-terminated counterpart. The present result provides a pathway for exploring exotic quantum phenomena utilizing the Fermi-arc properties of WSMs.

We thank D. Takane, N. Inami, H. Kumigashira, K. Ono, S. Ideta, and K. Tanaka for their assistance in ARPES measurements. This work was supported by MEXT of Japan (Innovative Area “Topological Materials Science”, Grant No. 15H05853), JSPS (KAKENHI 15H02105, 26287071, 25287079, 25220708, and Grant-in-Aid for JSPS Fellows 23.4376), KEK-PF (Proposals No. 2012S2-001 and No. 2015S2-003), and UVSOR (Proposal No. 25-536).

- [1] X. Wan, A. M. Turner, A. Vishwanath, and S. Y. Savrasov, *Phys. Rev. B* **83**, 205101 (2011).
 [2] L. Balents, *Physics* **4**, 36 (2011).
 [3] H. B. Nielsen and M. Ninomiya, *Phys. Lett. B* **130**, 389 (1983).

- [4] G. Xu, H. Weng, Z. Wang, X. Dai, and Z. Fang, *Phys. Rev. Lett.* **107**, 186806 (2011).
 [5] A. A. Burkov and L. Balents, *Phys. Rev. Lett.* **107**, 127205 (2011).

- [6] S. Murakami, *New J. Phys.* **9**, 356 (2007).
- [7] M. Hirayama, R. Okugawa, S. Ishibashi, S. Murakami, and T. Miyake, *Phys. Rev. Lett.* **114**, 206401 (2015).
- [8] P. Hosur and X.-L. Qi, *C. R. Phys.* **14**, 857 (2013).
- [9] A. A. Burkov, *J. Phys.: Condens. Matter* **27**, 113201 (2015).
- [10] H. Nielsen and M. Ninomiya, *Nucl. Phys. B* **185**, 20 (1981).
- [11] H. Nielsen and M. Ninomiya, *Nucl. Phys. B* **193**, 173 (1981).
- [12] A. A. Zyuzin and A. A. Burkov, *Phys. Rev. B* **86**, 115133 (2012).
- [13] C.-X. Liu, P. Ye, and X.-L. Qi, *Phys. Rev. B* **87**, 235306 (2013).
- [14] Z. Wang and S.-C. Zhang, *Phys. Rev. B* **87**, 161107(R) (2013).
- [15] Y. Chen, S. Wu, and A. A. Burkov, *Phys. Rev. B* **88**, 125105 (2013).
- [16] K. Landsteiner, *Phys. Rev. B* **89**, 075124 (2014).
- [17] M. N. Chernodub, A. Cortijo, A. G. Grushin, K. Landsteiner, and M. A. H. Vozmediano, *Phys. Rev. B* **89**, 081407 (2014).
- [18] P. Hosur, *Phys. Rev. B* **86**, 195102 (2012).
- [19] A. C. Potter, I. Kimchi, and A. Vishwanath, *Nat. Commun.* **5**, 5161 (2014).
- [20] H. Weng, C. Fang, Z. Fang, B. A. Bernevig, and X. Dai, *Phys. Rev. X* **5**, 011029 (2015).
- [21] S.-M. Huang, S.-Y. Xu, I. Belopolski, C.-C. Lee, G. Chang, B. Wang, N. Alidoust, G. Bian, M. Neupane, C. Zhang, S. Jia, A. Bansil, H. Lin, and M. Z. Hasan, *Nat. Commun.* **6**, 7373 (2015).
- [22] S.-Y. Xu, I. Belopolski, N. Alidoust, M. Neupane, G. Bian, C. Zhang, R. Sankar, G. Chang, Z. Yuan, C.-C. Lee, S.-M. Huang, H. Zheng, J. Ma, D. S. Sanchez, B. Wang, A. Bansil, F. Chou, P. P. Shibayev, H. Lin, S. Jia, and M. Z. Hasan, *Science* **349**, 613 (2015).
- [23] B. Q. Lv, H. M. Weng, B. B. Fu, X. P. Wang, H. Miao, J. Ma, P. Richard, X. C. Huang, L. X. Zhao, G. F. Chen, Z. Fang, X. Dai, T. Qian, and H. Ding, *Phys. Rev. X* **5**, 031013 (2015).
- [24] L. X. Yang, Z. K. Liu, Y. Sun, H. Peng, H. F. Yang, T. Zhang, B. Zhou, Y. Zhang, Y. F. Guo, M. Rahn, D. Prabhakaran, Z. Hussain, S.-K. Mo, C. Felser, B. Yan, and Y. L. Chen, *Nat. Phys.* **11**, 728 (2015).
- [25] B. Q. Lv, N. Xu, H. M. Weng, J. Z. Ma, P. Richard, X. C. Huang, L. X. Zhao, G. F. Chen, C. E. Matt, F. Bisti, V. N. Strocov, J. Mesot, Z. Fang, X. Dai, T. Qian, M. Shi, and H. Ding, *Nat. Phys.* **11**, 724 (2015).
- [26] S.-Y. Xu, N. Alidoust, I. Belopolski, Z. Yuan, G. Bian, T.-R. Chang, H. Zheng, V. N. Strocov, D. S. Sanchez, G. Chang, C. Zhang, D. Mou, Y. Wu, L. Huang, C.-C. Lee, S.-M. Huang, B. Wang, A. Bansil, H.-T. Jeng, T. Neupert, A. Kaminski, H. Lin, S. Jia, and M. Z. Hasan, *Nat. Phys.* **11**, 748 (2015).
- [27] N. Xu, H. M. Weng, B. Q. Lv, C. E. Matt, J. Park, F. Bisti, V. N. Strocov, D. Gawryluk, E. Pomjakushina, K. Conder, N. C. Plumb, M. Radovic, G. Autès, O. V. Yazyev, Z. Fang, X. Dai, T. Qian, J. Mesot, H. Ding, and M. Shi, *Nat. Commun.* **7**, 11006 (2016).
- [28] D. F. Xu, Y. P. Du, Z. Wang, Y. P. Li, X. H. Niu, Q. Yao, P. Dudin, Z.-A. Xu, X. G. Wan, and D. L. Feng, *Chin. Phys. Lett.* **32**, 107101 (2015).
- [29] I. Belopolski, S.-Y. Xu, D. S. Sanchez, G. Chang, C. Guo, M. Neupane, H. Zheng, C.-C. Lee, S.-M. Huang, G. Bian, N. Alidoust, T.-R. Chang, B. K. Wang, X. Zhang, A. Bansil, H.-T. Jeng, H. Lin, S. Jia, and M. Z. Hasan, *Phys. Rev. Lett.* **116**, 066802 (2016).
- [30] C. Shekhar, A. K. Nayak, Y. Sun, M. Schmidt, M. Nicklas, I. Leermakers, U. Zeitler, Y. Skourski, J. Wosnitza, Z. Liu, Y. Chen, W. Schnelle, H. Borrmann, Y. Grin, C. Felser, and B. Yan, *Nat. Phys.* **11**, 645 (2015).
- [31] Z. Wang, Y. Zheng, Z. Shen, Y. Zhou, X. Yang, Y. Li, C. Feng, and Z.-A. Xu, *Phys. Rev. B* **93**, 121112(R) (2016).
- [32] See Supplemental Material at <http://link.aps.org/supplemental/10.1103/PhysRevB.93.161112> for the details of the experimental conditions, the surface characterization, the band-structure calculations, and the ARPES-data analyses.
- [33] Y. Sun, S.-C. Wu, and B. Yan, *Phys. Rev. B* **92**, 115428 (2015).